Contents lists available at ScienceDirect

Applied Catalysis B: Environmental

Selective catalytic reduction of NO by H_2/C_3H_6 over $Pt/Ce_{1-x}Zr_xO_{2-\delta}$: The synergy effect studied by transient techniques

Christos M. Kalamaras[a], George G. Olympiou[a], Vasile I. Pârvulescu[b], Bogdan Cojocaru[b], Angelos M. Efstathiou[a,*]

[a] Department of Chemistry, Heterogeneous Catalysis Laboratory, University of Cyprus, University Campus, P.O. Box 20537, Nicosia 1678, Cyprus
[b] Department of Chemical Technology and Catalysis, University of Bucharest, 4-12 Regina Elisabeta Bvd., Bucharest, Romania

ARTICLE INFO

ABSTRACT

A series of $Pt/Ce_xZr_{1-x}O_{2-\delta}$ (x = 0.4–0.6) solids were synthesized and evaluated for the SCR of NO under lean burn conditions (2.5 vol% O_2) using C_3H_6 and H_2 as reducing agents. SSITKA-Mass Spectrometry, SSITKA-DRIFTS and other *in situ* DRIFTS experiments were conducted for the first time to gather fundamental information in explaining the remarkable H_2/C_3H_6 synergy effect towards steady-state selective reduction of NO into N_2 at T > 400 °C. In particular, the chemical structure of adsorbed *active* and *inactive* (spectator) NO_x species formed under C_3H_6-SCR, H_2-SCR and H_2/C_3H_6-SCR of NO and the surface coverage and site formation of *active* NO_x were probed. The $Pt/Ce_{1-x}Zr_xO_{2-\delta}$ catalysts present significant differences in their H_2-SCR performance (NO conversion and N_2-selectivity) in the low-temperature range of 120–180 °C but practically the same catalytic behavior at higher temperatures. It was proved that the *active* NO_x of the H_2-SCR path reside within a reactive zone around each Pt nanoparticle which extends to *less than one lattice constant* within the support surface. The chemical structure of the *active* intermediate was proved to be the *chelating nitrite*, whereas nitrosyl, monodentate and bidentate nitrates were considered as inactive species (spectators). It was illustrated for the first time that the presence of 15 vol% H_2O in the H_2-SCR feed stream applied over the 0.1 wt% $Pt/Ce_{0.5}Zr_{0.5}O_2$ catalyst results in a 25% decrease in the concentration of *active* NO_x, thus partly explaining the drop in activity observed when compared to the H_2-SCR in the absence of H_2O. A remarkable activity and N_2-selectivity enhancement was observed at T > 400 °C when both H_2 and C_3H_6 reducing agents were used compared to H_2-SCR or C_3H_6-SCR alone. This *synergy effect* was explained to arise mainly because of the increase of θ_H by the presence of $-CH_x$ species derived from adsorbed propylene decomposition on Pt, which block sites of oxygen chemisorption, and of the increase of surface oxygen vacant sites that promote the formation of a more active chelating nitrite (NO_2^-) species compared to the case of H_2-SCR.

1. Introduction

In spite of the fact that considerable research has been devoted to the selective catalytic reduction of NO_x by hydrocarbons under lean-burn conditions for mobile applications (HC-SCR) [1–6], this technology has not yet found application. Instead, the development of lean NO_x trap (LNT) for gasoline and of the urea-SCR for diesel vehicles (especially heavy-duty trucks) to meet current NO_x emissions standards are the current de-NO_x technologies, which are subjected to further improvements [4,7].

The beneficial role of H_2 in HC-SCR has first been reported on Ag-based catalysts [8–14] and recently only in C_3H_6-SCR over alumina-supported Pt, Pd and Ir catalytic systems [15]. Further investigations in HC/H_2-SCR with novel catalyst formulations for lean-burn applications, where H_2/HC reducing agents are found in the exhaust gas stream or can be produced on-board (e.g. diesel or gasoline lean burn engines) should therefore be considered. Low-temperature (120–200 °C) H_2-SCR on a 0.1 wt% Pt/CeO_2 catalytic system with a wide temperature window of operation (e.g. NO-conversion >50%) and N_2-selectivities in the 40–80%-range has been reported [16]. Furthermore, platinum-free WO_x-promoted $Ce_{1-x}Zr_xO_2$ solids were investigated for the first time towards H_2-SCR [17], where NO-conversions in the 30–50% range and N_2-selectivites larger than 80% were reported in the temperature range of 200–450 °C. These catalytic systems might be considered to

serve as reference for future catalyst developments (based on low-loading Pt or Pd) towards lean-burn applications, if modified ceria supports and the use of gas mixtures with an appropriate ratio of H_2/HC reducing agents of NO_x are used.

The role of C_3H_6, CO and H_2 on the efficiency and selectivity of NO_x storage reduction (NSR) process over a 2.1 wt% Pt/CeO_2-ZrO_2 catalyst has been investigated [18]. It was concluded that the presence of such reducing agents in the lean gas mixture can lead to the competition between NO_x storage and reduction steps. Also, the N_2O selectivity is a strong function of reaction temperature and reductant species [18]. In a recent work [6], temporal analysis of products (TAP) was used to study the NO reduction to N_2 over H_2- and C_3H_6-reduced (La, Zr)-doped CeO_2 at 560 °C with the goal to understand the lean de-NO_x catalytic chemistry by hydrocarbons. It was found [6] that a C_3H_6-reduced solid outperformed that of H_2-reduced owing to the deeper degree of reduction and the presence of carbonaceous deposits. No evidence was found that these carbonaceous residues play a direct role in the NO conversion. Their role was to extend the effectiveness of the catalyst in the conversion of NO under lean burn conditions by creating new oxygen vacancies responsible for the decomposition of NO into N_2 gas. The carbonaceous deposits are preferentially oxidized to CO_2 by lattice oxygen species of the (La, Zr)-doped CeO_2 solid [6].

In the present work we report the effect of the use of a mixture of H_2 and C_3H_6 reducing agents of NO in the presence of 2.5 vol% O_2 and in the 150–600 °C range over 0.1 wt% Pt supported on $Ce_{1-x}Zr_xO_{2-\delta}$ carriers. A strong remarkable synergy effect was found in the 450–600 °C range, which resulted practically in the complete conversion of NO into N_2 gas (N_2-selectivities >97%). At temperatures lower than 450 °C, the H_2-SCR appears as the most effective de-NO_x process over this catalytic system. In order to promote the fundamental knowledge on the intrinsic reasons that lead to the observed remarkable synergy effect between H_2 and C_3H_6 towards NO_x reduction, SSITKA (use of ^{15}NO isotope gas) coupled with *in situ* Mass Spectrometry and DRIFTS and other transient experiments were conducted for the first time. In particular, the focus of the present investigation was to obtain information on important kinetic parameters, such as: (a) the chemical structure of adsorbed *active* and *inactive* (spectator) NO_x species under C_3H_6-SCR, H_2-SCR and H_2/C_3H_6-SCR and (b) the surface coverage and location (Pt or support) of *active* NO_x.

2. Experimental

2.1. Catalyst preparation

The synthesis of $Ce_{1-x}Zr_xO_{2-\delta}$ supports (x = 0.4-0.6 or Ce/Zr = 0.67–1.5) was carried out using the citrate sol-gel method. Appropriate amounts of $Ce(NO_3)_3$ (Fluka) and $ZrO(NO_3)_2$ (Across) were dissolved in water and citric acid ($C_6H_8O_7 \cdot H_2O$, Merck) was then added under continuous stirring. The resulting solution was stirred under vacuum for gradual evaporation of water at 60 °C. The final gel was dried under CO_2 supercritical conditions (180 atm and 80 °C) and the solid product obtained was then calcined in air from room T to 500 °C at the heating rate of 0.5 °C min^{-1}. The supported Pt catalysts were prepared by impregnating the $Ce_{1-x}Zr_xO_{2-\delta}$ supports with a given amount of aqueous solution of $H_2Pt^{IV}Cl_6$ (Aldrich) so as to obtain the desired 0.1 wt% Pt loading. After gradual evaporation of water at 70 °C for 4 h, the resulting slurry was dried at 120 °C overnight and then calcined in a furnace (ELF 11/6, Carbolite, static air) at 500 °C for 2 h (heating rate of 50 °C min^{-1} from 25 to 500 °C). Prior to any catalytic measurements, the fresh catalyst sample was pretreated with 20 vol% O_2/He (50 NmL min^{-1}) at 500 °C for 2 h followed by reduction in 25 vol% H_2/He (50 NmL min^{-1}) at 220 °C for 2 h.

2.2. Catalyst characterization

2.2.1. Textural and X-ray diffraction studies

The $Ce_{1-x}Zr_xO_{2-\delta}$ supports were characterized for their texture by the physical adsorption method (adsorption of N_2 at 77 K) using a Micromeritics Gemini III surface area and pore size analyzer. The specific surface area (SSA, m^2 g^{-1}, BET method) of the solid supports was measured after the sample was degassed in N_2 gas at 350 °C for 2 h. The primary mean crystallite size of the $Ce_{1-x}Zr_xO_{2-\delta}$ solids was estimated from powder XRD studies (particles in powder form with less than 100 μm in size; Shimadzu 6000 diffractometer using Cu Kα radiation (λ = 1.5418 Å)) and after using the Scherrer formula. X-ray diffractograms were recorded in the 10–80° 2θ range with a step scan of 2° min^{-1}. *In situ* XRD studies were performed over the fresh catalyst samples after treatment with a 20 vol% O_2/He (50 NmL min^{-1}/2 h) gas mixture in the 200–600 °C range followed by 25 vol% H_2/He (50 NmL min^{-1}/2 h) gas treatment in the 200–600 °C range.

2.2.2. X-ray photoelectron spectroscopy (XPS) and Raman studies

The surface oxidation state and composition (atom-%) of cerium in the three $Ce_{1-x}Zr_xO_{2-\delta}$ – supported Pt (x = 0.4–0.6 or Ce/Zr = 0.67–1.5) solids was investigated by X-ray photoelectron spectroscopy (XPS, Kratos Axis). The excitation was performed by using a conventional dual anode X-ray source (Specs XR 50, Mg K_α line (1253.6 eV)). Fitting and integration of X-ray photoelectron peaks were performed by using the commercial software CASAXPS (CASA software Ltd). Raman spectroscopy was used to characterize the oxygen sub-lattice of $Ce_{1-x}Zr_xO_{2-\delta}$ solids before and after reaction conditions (*ex situ*). Raman spectra were recorded using a Horiba Jobin Yvon-Labram HR UV–vis-NIR (200–1600 nm) Raman Microscope Spectrometer and a laser with a wavelength of 632 nm. The spectra recorded were the average of 10 scans at the resolution of 2 cm^{-1}.

2.2.3. H_2 temperature-programmed desorption (TPD) studies

The dispersion of Pt metal in the 0.1 wt% $Pt/Ce_{1-x}Zr_xO_{2-\delta}$ solids was determined by selective H_2 chemisorption at 25 °C followed by temperature-programmed desorption (TPD) in He flow (30 NmL min^{-1}) previously described [19,20]. A 0.5-g fresh catalyst sample was first calcined in a 20 vol% O_2/He gas mixture (50 NmL min^{-1}) at 500 °C for 2 h and then reduced in pure H_2 (50 NmL min^{-1}) at 220 °C for 2 h. Quantitative analysis of the effluent gas stream from the microreactor was performed using an *on line* quadrupole mass spectrometer (Omnistar, Balzers) equipped with a fast response inlet capillary/leak valve (SVI050, Balzers) and data acquisition systems. A H/Pt_s = 1 for hydrogen chemisorption stoichiometry was considered.

2.3. Catalytic performance studies

The gas flow-system used for performing catalytic studies consisted of a flow measuring and control system (mass flow controllers, MKS Instruments, Model 47C), mixing chambers and a quartz fixed-bed microreactor (∼ 2 mL nominal volume) [19,21]. Analysis of the dry effluent gas stream from the reactor was performed using mass spectrometer (Balzers, model Omnistar, amu = 1-300) for H_2 (m/z = 2) and O_2 (m/z = 32) and NO_x chemiluminesence analyzer (Thermo Electron Corporation, model 42C) for NO and NO_2. An *on line* infrared gas analyzer (Teledyne Analytical Instruments, model IR 7000) was used for the measurement of N_2O [22]. A mass of 0.3 g of catalyst (powder, 0.1 < d_p < 0.2 mm) and a total volume flow rate of 200 NmL min^{-1}, resulting in a GHSV of 33,000 h^{-1} (L/$L_{cat.bed}$/h) were used. The feed concentrations regarding NO and O_2 were kept constant at the level of 150 ppm and 2.5 vol%, respectively, whereas those of H_2 and C_3H_6

reducing agents were 0.8 vol% and 0.5 vol%, respectively. Catalytic performance evaluation in the presence of CO_2 (10 vol%) and H_2O (15 vol%) was also conducted. No external or internal mass transport resistances were noticed under the above mentioned applied catalytic reaction performance testing conditions.

The fresh (as synthesized) catalyst sample was first pretreated in 20 vol% O_2/He gas mixture (50 NmL min^{-1}) at 500 °C for 2 h and then in 25 vol% H_2/He (50 NmL min^{-1}) at 220 °C for 2 h. The reductant/oxidant ratio used in several feed gas compositions is calculated using the following Eq. (1), which is based on the full reduction of NO_x into N_2:

$$red/ox = \frac{9\,[C_3H_6] + [H_2]}{[NO_x] + 2\,[O_2]} \tag{1}$$

In the case where water was used in the reaction feed gas stream, some ammonia formation was noticed in the condensate after passing the effluent stream from the reactor to a condenser (Peltier Gas Cooler, model ECP1000, M&C TechGroup) [22]. Quantification of ammonia in the condensate was performed using UV spectroscopy (Thermo Scientific, Model Helios-Beta) and available commercial kits (Merck, Product Number 100683).

2.4. In situ DRIFTS studies

A Perkin-Elmer Frontier FTIR spectrometer equipped with a high-temperature/high-pressure temperature controllable DRIFTS cell (Harrick, Praying Mantis) were used to in situ record infrared spectra obtained under reaction conditions. The spectrum of the solid was taken in Ar gas flow at the desired reaction temperature following catalyst pretreatment (20 vol% O_2/Ar at 500 °C for 2 h followed by 25 vol% H_2/Ar at 220 °C for 2 h), and this was subtracted from the spectrum of the solid recorded under the reaction gas mixture at the same temperature. DRIFTS spectra were collected in the 400–4000 cm^{-1} range at the rate of 1 scan s^{-1}, 2 cm^{-1} resolution and after a signal averaging was set to 50 scans per spectrum. DRIFTS spectra were smoothed to remove high-frequency noise, if necessary, and were further analyzed using the software Spectrum in accordance with guidelines reported [23].

2.5. SSITKA-mass spectrometry-DRIFTS studies

SSITKA-Mass Spectrometry experiments were performed in a specially designed transient gas flow-system [19,24,25]. The amount of catalyst used was varied so as to keep the NO conversion below 15%. The total amount of catalytic bed material was set to 0.3 g in all SSITKA experiments, after the active catalytic component was diluted with silica. The total flow rate was kept constant at 200 NmL min^{-1}. The reaction mixture consisted of 150 ppm NO, 2.5 vol% O_2, 0.8 vol% H_2 and/or 0.5 vol% C_3H_6 and He as balance gas. The SSITKA experiment involved the switch from the $^{14}NO/H_2/O_2/Ar/He$ to the equivalent isotopic $^{15}NO/H_2/O_2/He$ gas mixture after steady- state was achieved; the Ar gas was used as a tracer to monitor the system's gas-phase hold-up [24,25]. In the case of use of water in the feed gas stream, the effluent wet gas from the reactor was first passed through a condenser (Peltier system of low volume), the exit of which (dry gas) was directed to the mass spectrometer. The normal and isotope-containing reactants and products (e.g. ^{14}NO, ^{15}NO, $^{14}N_2$, $^{15}N_2$, $^{14}N^{15}N$, $^{14}N_2O$, $^{14}N^{15}NO$, and $^{15}N_2O$) were all monitored by on line mass spectrometry. More details on the SSITKA experiments were previously reported [26–28]. SSITKA-DRIFTS experiments were performed in a DRIFTS reactor cell having a response time (τ, s) of ~5 s at the flow rate of 200 NmL min^{-1}. Signal averaging was set to 50 scans per spectrum and the spectra were collected in the 4000–500 cm^{-1} range at the rate of 0.2 scans s^{-1} (MCT detector, resolution 2 cm^{-1}).

Table 1
Textural properties, platinum dispersion (D_{Pt}, %) and mean particle size (d_{Pt}, nm) of 0.1 wt% Pt/$Ce_{1-x}Zr_xO_{2-\delta}$ (x = 0.4–0.6) catalysts.

Catalyst	SSA (m^2 g^{-1})	d_p (nm)	D_{Pt} (%)[a]	d_{Pt} (nm)[a]
Pt/$Ce_{0.6}Zr_{0.4}O_{2-\delta}$	86	6.2	85	1.9
Pt/$Ce_{0.5}Zr_{0.5}O_{2-\delta}$	58	6.3	77	2.1
Pt/$Ce_{0.4}Zr_{0.6}O_{2-\delta}$	90	3.4	83	2.0

[a] Obtained after using the H_2-TPD technique (Section 2.2.3).

3. Results and discussion

3.1. Catalysts characterization

3.1.1. Textural properties and Pt particle size

Table 1 reports textural properties of the 0.1 wt% Pt/$Ce_{1-x}Zr_xO_{2-\delta}$ (x = 0.4, 0.5 and 0.6) catalysts investigated. The Pt/$Ce_{0.4}Zr_{0.6}O_{2-\delta}$ exhibits the highest SSA (90 m^2 g^{-1}) and the smallest mean pore diameter (d_p = 3.4 nm) compared to the other catalysts. The presence of mesoporosity is evidenced for all three solids with a mean pore diameter in the 3.4–6.3 nm range. The platinum dispersion (D_{Pt}, %) and the mean Pt particle size estimated (based on spherical geometry) for the Pt/$Ce_{1-x}Zr_xO_{2-\delta}$ catalysts are also reported in Table 1. It is clearly seen that dispersion of platinum changes only slightly and the corresponding mean Pt particle size (ca. 1.9–2.1 nm) appears similar to within 10% for all three supported Pt catalysts.

3.1.2. Bulk and surface structure

Powder X-ray diffraction patterns of fresh $Ce_{0.4}Zr_{0.6}O_{2-\delta}$, $Ce_{0.5}Zr_{0.5}O_{2-\delta}$ and $Ce_{0.6}Zr_{0.4}O_{2-\delta}$ solids are presented in Fig. 1a. On the basis of these results, a pseudo-cubic crystalline single phase $Ce_{1-x}Zr_xO_{2-\delta}$ solid solution is revealed [29–33]. Raman studies that follow confirm the presence of a single homogeneous phase of $Ce_{1-x}Zr_xO_{2-\delta}$. The X-ray diffraction peaks were slightly shifted to higher 2θ values after increasing the Zr content from x = 0.4 to 0.6, which indicates reduction in the lattice constant (α, Å) of the $Ce_{1-x}Zr_xO_{2-\delta}$ crystal lattice, which is the result of the introduction of Zr^{4+} into the CeO_2 fluorite matrix. This is due to the fact that the ionic radius of Zr^{4+} (0.84 Å) is smaller compared with that of Ce^{4+} (0.97 Å) and as a result of this the lattice constant (α) is reduced [32,33].

The mean primary crystal size (d_c, nm) of the $Ce_{1-x}Zr_xO_{2-\delta}$ solid solution following calcination (20% O_2/He, 750 °C/2 h) was found to be 4.3, 4.3 and 5.7 nm for the $Ce_{0.4}Zr_{0.6}O_{2-\delta}$, $Ce_{0.5}Zr_{0.5}O_{2-\delta}$ and $Ce_{0.6}Zr_{0.4}O_{2-\delta}$ solids, respectively. These results lead to the conclusion that all three $Ce_{1-x}Zr_xO_{2-\delta}$ solid supports were of nano-crystalline structure. It should be also noted that after de-NO_x catalytic performance experiments (120–600 °C, 20 h), all three $Ce_{1-x}Zr_xO_{2-\delta}$ solid solution supports maintained their nano-crystalline structure.

Raman studies were performed on the $Ce_{1-x}Zr_xO_{2-\delta}$ solids in order to investigate whether single micro-phases of ceria, zirconia or tetragonal t' phase of $Ce_{1-x}Zr_xO_{2-\delta}$ were formed, which are difficult to be evidenced by powder XRD. The Raman spectra obtained are reported in Fig. 1b. On the basis of these results and Raman spectra reported for pure ceria and zirconia phases [34,35], it is proved that in all three solids no pure single-phase CeO_2 or ZrO_2 is present. All samples maintain a cubic ceria-like structure due to the appearance of the relatively strong band at 460–468 cm^{-1}. This band is characteristic of the F2 g mode of the cubic fluorite-like structure, while that at 630 cm^{-1} is attributed to a non-degenerate longitudinal optical (LO) mode of ceria induced by the oxygen vacancies in the ceria lattice as the result of doping of ceria with Zr^{4+} [36,37]. The shift observed with the increase of the Zr content is a consequence of the lattice contraction brought by zirconium ion insertion

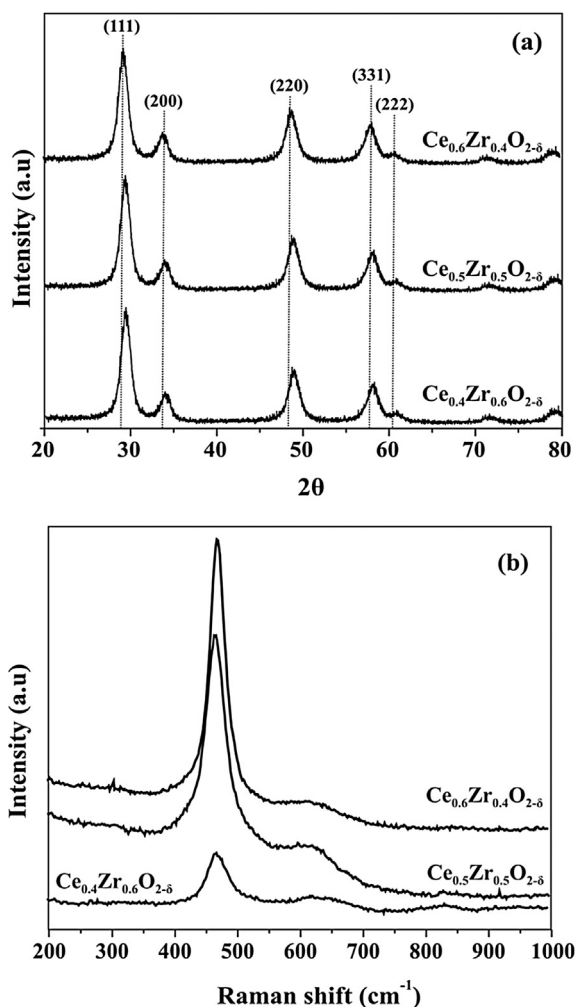Fig. 2. X-ray photoelectron spectra of the Ce 3d core levels of the $Pt/Ce_{1-x}Zr_xO_{2-\delta}$ (x = 0.4, 0.5 and 0.6) solids after 5 h in H_2-SCR ($NO/H_2/O_2$ reaction).

Fig. 1. (a) Powder X-ray diffraction patterns and (b) Raman spectra obtained over $Ce_{1-x}Zr_xO_{2-\delta}$ solids (x = 0.4, 0.5 and 0.6).

[37]. According to the literature [38], for the tetragonal phases t, t', and t'', with the same space group P42/nmc, six Raman modes near 131, 247, 307, 464, 596 and 626 cm^{-1} are allowed. The line at 307 cm^{-1} is related to the displacement of oxygen atoms from their ideal fluorite lattice positions (assigned to the pseudo-cubic or t'' phase [39]). The spectra collected for the investigated catalysts do not show this line which should appear for such a structure. The other potential Raman shifts would be overlapped by the intense lines at 464, 596 and 626 cm^{-1} corresponding to the cubic phase of the mixed CeO_2-ZrO_2 oxide. However, while Raman scattering from lattice vibrations is sensitive to the tetragonal distortion of the oxygen positions and contributes to distinguish between the c and t'' phases, the t' and t'' phases can be differentiated in principle from each other by powder XRD, where the presence of t' phase is evidenced by the spliting of the lines assigned to the (400) and (004) facets [38]. The XRD patterns recorded in the present work did not evidence such a splitting.

In summary, the Raman spectra shown in Fig. 1b are indicative of $Ce_{1-x}Zr_xO_{2-\delta}$ solid solutions (x = 0.4-0.6), where Zr^{4+} was incorporated into the ceria lattice resulting in distortions and lowering of symmetry for the ceria cubic structure but with no pure ceria or zirconia micro-crystalline phase formed.

Fig. 2 presents XP spectra of the Ce 3d core level for the three solids investigated after 5 h in H_2-SCR ($NO/H_2/O_2$ reaction) in the 120–300 °C range. According to the literature [40–44], the XP spectrum of Ce 3d in Ce^{4+}- o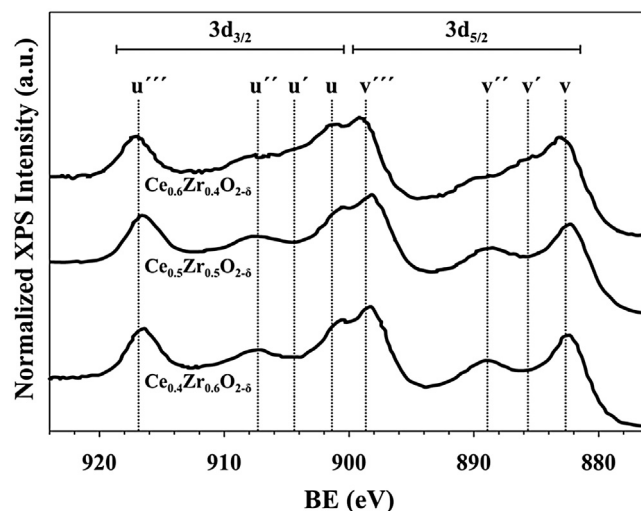xides shows six peaks (three pairs of spin-orbit doublets), whereas that of Ce^{3+}- oxide exhibits four peaks (two pairs of spin-orbit doublets). The Ce $3d_{3/2}$ multiplets are labeled u, whereas those of $3d_{5/2}$ are labeled v. In the case of pure Ce^{4+}- oxide, v, v'' and v''' peaks for the Ce $3d_{5/2}$ core level and u, u'' and u''' peaks for the Ce $3d_{3/2}$ level can be identified in its XP spectrum (from low to high binding energy). For pure Ce^{3+} oxide, v' corresponds to the Ce $3d_{5/2}$ core level and u' to the Ce $3d_{3/2}$ core level.

The u''' and v''' features could be assigned to the $3d^94f^0$ (Ce^{4+}) photoemission final state, the (v, v'') and (u, u'') doublets to the final states of strong $3d^94f^2$ and $3d^94f^1$ mixing (Ce^{4+}), whereas the v' and u' are unique features of the Ce^{3+} state. Similar XP spectra of the Ce 3d core level were reported over CeO_2-ZrO_2 solid solutions [43,45–47]. The Ce $3d_{3/2}$ and Ce $3d_{5/2}$ peak areas and amplitudes increased with increasing cerium concentration. This is attributed to the increasing cerium concentration since the amplitude and area of XPS photoemission features are proportional to the surface composition. The difference in Ce $3d_{3/2}$ and Ce $3d_{5/2}$ binding energies is also in agreement with the expected value of 18.6 eV. Examination of the Ce $3d_{3/2}$ and Ce $3d_{5/2}$ photoemission features indicates a slight chemical shift to a higher binding energy (0.3–0.4 eV) after increasing the cerium concentration from 60 to 40 atom-%. Although a slight binding energy shift is observed with changing composition, the shift is suggested to arise from the changing surface electronic structure independent of the oxidation state [47].

To verify the surface oxidation state of cerium as a function of the composition of $Ce_{1-x}Zr_xO_{2-\delta}$ mixed metal oxide, the peaks characteristic of Ce^{3+} (u', v') and Ce^{4+} (u''', v''') were further studied. In particular, the relative amount of Ce^{3+} in the samples was estimated from the %-area of u''' peak in the total Ce 3d region compared with reference values corresponding to the compounds of $CeAlO_3/Al_2O_3$ and $Ce(OH)_4$, which contain cerium in only the Ce^{4+} or Ce^{3+} oxidation state, respectively, and after assuming a linear dependence between %-u''' and Ce^{3+} composition [48]. It was found that 16.7, 15.0 and 17.4% of cerium atoms are in the Ce^{3+} state in the case of $Pt/Ce_{0.4}Zr_{0.6}O_{2-\delta}$, $Pt/Ce_{0.5}Zr_{0.5}O_{2-\delta}$ and $Pt/Ce_{0.6}Zr_{0.4}O_{2-\delta}$ solids, respectively. The latter result indicates a practically constant concentration of surface Ce^{3+} defect sites independent of zirconium substitution (in the range x = 0.4–0.6). It is important to note that for the fresh surface state of $Pt/Ce_{0.6}Zr_{0.4}O_{2-\delta}$ (e.g. the catalyst was first reduced in 25 vol% H_2/He (50 NmL min^{-1}) at 220 °C for 2 h before H_2-SCR), 42.4% of Ce atoms were found in the Ce^{3+} oxidation state
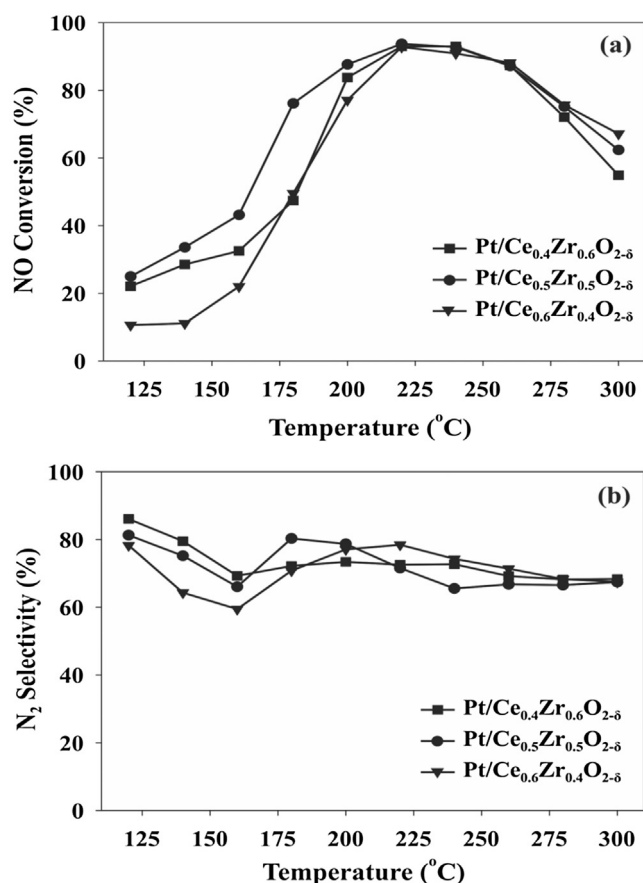
Fig. 3. Effect of support chemical composition and reaction temperature (120–300 °C) on the (a) X_{NO} (%) and (b) S_{N2} (%) of H_2-SCR over the 0.1 wt% Pt/$Ce_{1-x}Zr_xO_{2-\delta}$ (x = 0.4, 0.5 and 0.6) catalysts. GHSV = 33,000 h^{-1}; feed gas composition: 150 ppm NO/0.8 vol% H_2/2.5 vol% O_2/He.

Fig. 4. Catalytic performance in terms of (a) X_{NO} (%), (b) S_{N2} (%) and S_{NH3} (%) of the 0.1 wt% Pt/$Ce_{0.5}Zr_{0.5}O_{2-\delta}$ solid in the 180–320 °C range. Feed gas compositions used: 150 ppm NO/0.8 vol% H_2/2.5 vol% O_2/He; 150 ppm NO/0.8 vol% H_2/2.5 vol% O_2/10 vol% CO_2/He; 150 ppm NO/0.8 vol% H_2/2.5 vol% O_2/10 vol% CO_2/15 vol% H_2O/He; GHSV = 33,000 h^{-1}.

compared with the value of 17.4% obtained after H_2-SCR (5 h on stream). The latter result is similar to the work of Wu et al. [43] who have shown a significant decrease (∼90%) in the %-Ce^{3+} composition in the $Ce_{1-x}Zr_xO_{2-\delta}$ mixed metal oxides after calcination at 1000 °C for 20 h. The high concentration of Ce^{3+} in the fresh sample should be largely related to the defect sites formed during synthesis and to a lesser extent after hydrogen reduction at 220 °C [49].

3.2. Catalytic activity measurements

3.2.1. H_2-SCR
3.2.1.1. The effect of support chemical composition (Ce/Zr ratio). Fig. 3 presents the effect of $Ce_{1-x}Zr_xO_{2-\delta}$ support chemical composition (x = 0.4–0.6) on the catalytic activity, in terms of NO conversion (X_{NO}, %) and N_2-selectivity (S_{N2}, %) of the 0.1 wt% Pt/$Ce_xZr_{1-x}O_{2-\delta}$ solids in the 120–300 °C range after using the feed gas composition: 150 ppm NO/0.8 vol% H_2/2.5 vol% O_2/He (H_2-SCR) with an equivalent red/ox ratio of 0.16 (Eq. (1)). It is observed that the three catalyst compositions exhibit similar trends and features for the X_{NO} (%) profiles (volcano type) with the same maximum activity of ∼92% at 220 °C. However, in the low-temperature range of 120–200 °C, the Pt/$Ce_{0.5}Zr_{0.5}O_{2-\delta}$ solid presents significantly higher catalytic activity compared with the other solids. In particular, at 180 °C the X_{NO} = 75% to be compared to 48% obtained with the other two catalytic compositions. At temperatures higher than 200 °C, all three catalysts show very similar activity behavior (within 10%-units, Fig. 3a). The N_2-selectivity profile behavior of all three catalysts appears to be similar (Fig. 3b) with maximum selectivity values difference of 15%-units.
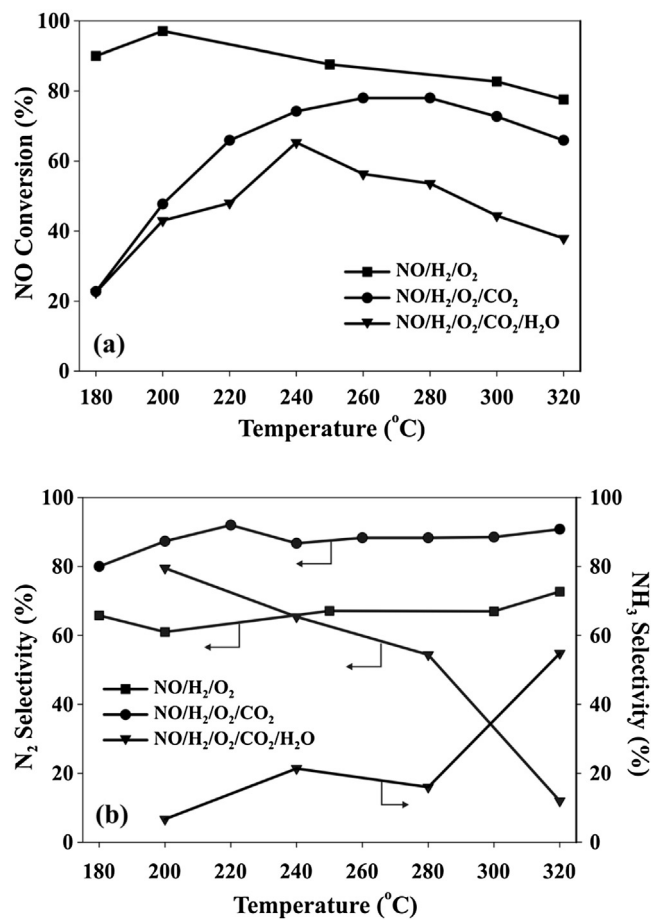
In order to check the effect of any chlorine left on the supported 0.1 wt% Pt catalysts after calcination and reduction (see Section 2.1), the $Ce_{0.6}Zr_{0.4}O_2$ support material was also impregnated with the appropriate amount of Pt(NO_2)$_2$(NH_3)$_2$ (Aldrich) solution in distilled and de-ionized water, free of chlorine. All drying, calcination and reduction steps were kept the same as in the case of use of $H_2Pt^{IV}Cl_6$ solution. Hydrogen chemisorption followed by TPD (see Section 2.2.3) showed a very similar trace as that observed with the corresponding catalyst sample when $H_2Pt^{IV}Cl_6$ was used to deposit Pt, thus implying a very similar metal dispersion. The H_2-SCR catalytic performance test for the conditions reported in Fig. 3 resulted also in very similar X_{NO} vs T and S_{N2} vs T profiles, all within 3–5%.

3.2.1.2. The effect of CO_2 and H_2O in the H_2-SCR. Fig. 4 presents the catalytic performance in terms of NO-conversion, X_{NO} (%) (Fig. 4a), N_2-selectivity, S_{N2} (%) and NH_3-selectivity, S_{NH3} (%) (Fig. 4b) obtained over the 0.1 wt% Pt/$Ce_{0.5}Zr_{0.5}O_{2-\delta}$ solid in the 180–320 °C range after using an H_2-SCR feed gas composition containing also CO_2 (150 ppm NO/0.8 vol% H_2/2.5 vol%O_2/10 vol% CO_2/He) or CO_2 and H_2O (150 ppm NO/0.8 vol% H_2/2.5 vol%O_2/10 vol% CO_2/15 vol% H_2O/He) and having the same GHSV (33,000 h^{-1}) and red/ox ratio (0.16) as of Fig. 3. In addition to N_2 and N_2O nitrogen-containing gas products, only in the case when water is present in the feed NH_3 is also formed. The latter result agrees very well with the work of Masdrag et al. [18] obtained under lean burn de-NO_x conditions over similar catalytic systems. It is seen that the presence of CO_2 in the feed gas stream has a significant negative effect, where a drop by

20–70%-units in the X_{NO} (%) is obtained in the 180–240 °C range. On the other hand, at T > 260 °C, only a small decrease (by 10%-units) is observed (Fig. 4a). Furthermore, the presence of CO_2 in the feed stream results in a significant improvement of N_2-selectivity (Fig. 4b). This effect of CO_2 on the activity and N_2-selectivity was previously reported over the Pt/MgO-CeO$_2$ catalytic system for similar feed gas compositions [22]. It was suggested that the presence of CO_2 blocks preferentially active but largely non-selective NO_x adsorption sites on the support close to the Pt nanoparticle-support interface (forming adsorbed carbonate-like species). The location of active NO_x intermediate species for the present catalytic systems is also probed (see Section 3.3.1.1), where the former lie within a reactive zone of ∼2 Å from the periphery of Pt in contact with the $Ce_{0.5}Zr_{0.5}O_{2-\delta}$ support as was in the case of Pt/MgO-CeO$_2$ catalytic system (∼5 Å) [26].

In the case where both CO_2 and H_2O are present in the feed gas stream, a further drop in catalytic activity is observed; a maximum NO conversion of 65% is obtained at 240 °C compared to 97% at 200 °C when no CO_2 and H_2O are present in the feed. On the other hand, at T < 240 °C the presence of H_2O in the feed is found to improve S_{N2}, while a large decrease is seen at T > 240 °C due to the formation of NH_3 (Fig. 4b). The low NO conversion values may be attributed to the competitive adsorption of H_2O and NO on support surface sites. This is supported by SSITKA-MS experiments to be reported in the following Section 3.3, where the presence of H_2O in the feed stream results in a 25% decrease in the concentration of active NO_x intermediates. However, the improved N_2-selectivity behavior observed at low temperatures (T < 240 °C) could be explained by the fact that H_2O stabilizes active NO_3^- adsorbed species and at the same time dissociative adsorption of H_2O increases the surface concentration of H onto the support. The latter kinetic parameter is considered important for the NO_x reduction step [22].

3.2.2. H$_2$/C$_3$H$_6$-SCR

Fig. 5 presents the effect of reaction temperature in the 150–600 °C range on the X_{NO} (%) and S_{N2} (%) for the reduction of NO using both H_2 and C_3H_6 as reducing agents (red/ox = 1.06). For strict comparison, results are presented when H_2 (red/ox = 0.16) or C_3H_6 (red/ox = 0.9) alone is used as reducing agent. It is clearly observed that the use of C_3H_6 alone (C_3H_6-SCR) results in significantly lower NO conversion values than when H_2 alone is used (H_2-SCR). In particular, at 200 and 500 °C, H_2-SCR results in X_{NO} values of 97 and 50%, whereas C_3H_6-SCR in X_{NO} values of 10 and 5%, respectively. In both cases, a volcano-type activity profile is obtained but the maximum conversion of NO occurs at a significantly lower temperature in the case of H_2-SCR (ca. 200 °C) compared to the case of C_3H_6-SCR (ca. 350 °C). Very similar volcano-type activity profiles to those shown in Fig. 5a have been recently reported on 0.5 wt% Pt/γ-Al$_2$O$_3$ [15] using a larger concentration of NO in the feed (ca. 1000 ppm) but lower concentration of C_3H_6 (0.1 vol%) and H_2 (0.5 vol%) and similar O_2 concentration (2 vol%) and GHSV (40,000 h^{-1}). In the latter work [15] maximum NO-conversion in H_2-SCR and C_3H_6-SCR occurred at lower temperatures compared to the present case (Fig. 5a). Regarding the N_2-selectivity behavior of the present Pt/Ce$_{0.5}$Zr$_{0.5}$O$_2$ catalyst (Fig. 5b), this was found to be larger in the case of C_3H_6-SCR than H_2-SCR for several reaction temperatures in the 150–600 °C range.

When both H_2 and C_3H_6 were present in the feed, a remarkable increase in both the NO-conversion and N_2-selectivity is obtained in the 400–600 °C range (Fig. 5a,b) compared to H_2-SCR or C_3H_6-SCR. This implies the existence of a *synergy effect* between H_2 and C_3H_6. According to *in situ* DRIFTS studies to be presented in the following Section 3.3, the presence of H_2 in the feed stream leads to a significant increase in the surface coverage of adsorbed –CH$_x$ species on Pt and support, where oxidation of these –CH$_x$ species to

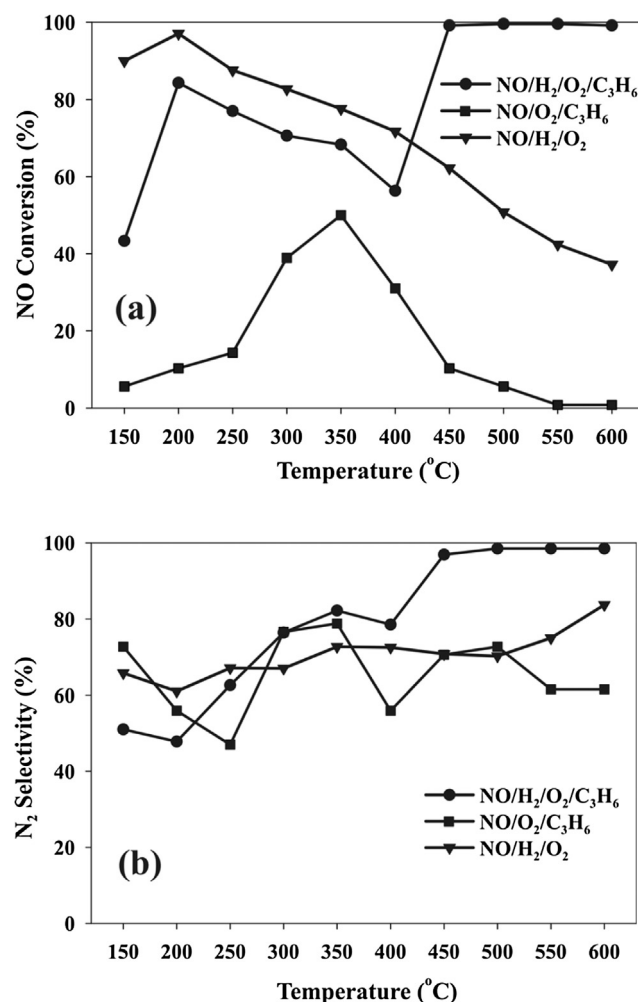**Fig. 5.** Catalytic performance in terms of (a) X_{NO} (%) and (b) S_{N2} (%) of the 0.1 wt% Pt/Ce$_{0.5}$Zr$_{0.5}$O$_{2-\delta}$ solid in the 150–600 °C range for the selective catalytic reduction of NO using H_2/C_3H_6 gas mixture as reducing agents. GHSV = 33,000 h^{-1}; feed gas compositions: 150 ppm NO/0.8 vol% H_2/2.5 vol% O_2/He; 150 ppm NO/0.5 vol% C_3H_6/2.5 vol% O_2/He; 150 ppm NO/0.8 vol% H_2/0.5 vol% C_3H_6/He.

CO_2 and H_2O on Pt facilitates back spillover of labile surface oxygen located at the Pt-Ce$_{1-x}$Zr$_x$O$_{2-\delta}$ interface. This in turn leads to the formation of oxygen vacancies within the active reaction zone around the Pt nanoparticles [6], which seem to participate in the formation of *more active chelating nitrites*. The present results (Fig. 5) demonstrate that H_2 contributes to a greater extent than C_3H_6 in the lean SCR of NO_x in harmony with the recent work of Goula et al. [15] performed over a 0.5 wt% Pt/γ-Al$_2$O$_3$ catalyst. On the other hand, the present Pt/Ce$_{0.5}$Zr$_{0.5}$O$_2$ catalytic system leads to a remarkable synergy effect between H_2 and C_3H_6 in bringing both X_{NO} and S_{N2} at T > 400 °C to the largest possible value, result not reported in the case of Pt/γ-Al$_2$O$_3$ [15].

3.3. Mechanistic studies

3.3.1. H$_2$-SCR of NO

3.3.1.1. SSITKA-mass spectrometry studies. The surface concentration (μmol g^{-1}) and surface coverage, θ_{NOx} (based on the surface Pt atoms) of the active NO_x reaction intermediates, which are found in the nitrogen-path of the NO/H$_2$/O$_2$ (H$_2$-SCR) reaction in the 200–300 °C range and are responsible for the formation of N_2 and N_2O, were determined by SSITKA-Mass spectrometry experiments (use of ^{15}NO). Fig. 6a shows dimensionless concentration
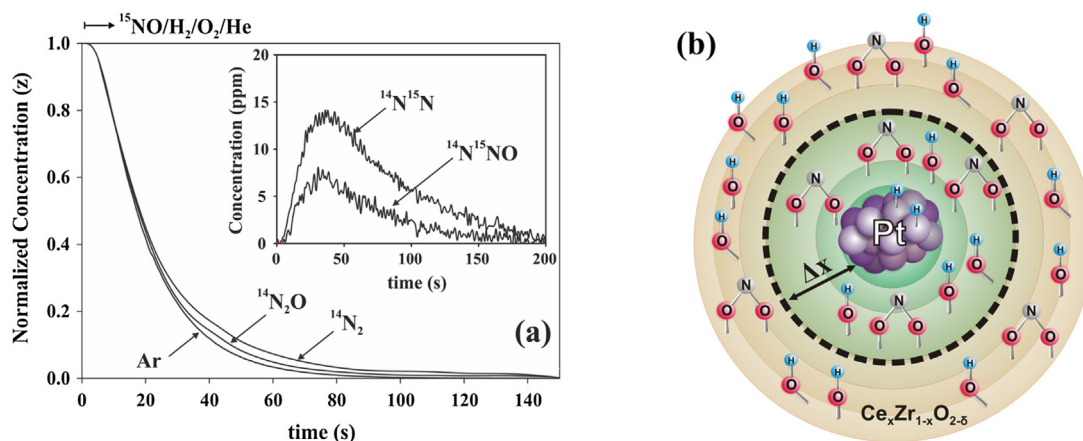
Fig. 6. (a) Transient response curves of $^{14}N_2$, $^{14}N^{15}N$, $^{14}N_2O$, $^{14}N^{15}NO$ and Ar obtained during SSITKA-mass spectrometry experiments ($^{14}NO/H_2/O_2/Ar/He \rightarrow {}^{15}NO/H_2/O_2/He$) at 200 °C over the 0.1 wt% Pt/Ce$_{0.5}$Zr$_{0.5}$O$_{2-\delta}$ catalyst; (b) The extent (Δx, Å) of reactive zone around each Pt nanoparticle within which *active* NO$_x$ in the N-path of H$_2$-SCR are formed over Pt/Ce$_x$Zr$_{1-x}$O$_{2-\delta}$ catalysts.

Table 2
Concentration (μmol g^{-1}) and surface coverage (θ_N) of the *active* "N-containing" species obtained during H$_2$-SCR over the 0.1 wt% Pt/Ce$_{0.5}$Zr$_{0.5}$O$_{2-\delta}$ catalyst at 200, 250 and 300 °C.

T (°C)	"N-pool" (μmol g^{-1})	θ_N[a]
200	14.1	3.6
250	7.2 (5.4)[b]	1.8 (1.4)[b]
300	17.5	4.4

[a] Number of Pt monolayers (based on the exposed Pt$_s$).
[b] Concerns the switch $^{14}NO/H_2/O_2/H_2O \rightarrow {}^{15}NO/H_2/O_2/H_2O$.

[24,25] transient response curves (Z) of the $^{14}N_2$ and $^{14}N_2O$ formation rates as well as transient concentration evolution curves of $^{14}N^{15}N$ and $^{14}N^{15}NO$ formation (inset graph, Fig. 6a) after the switch $^{14}NO/H_2/O_2/He/Ar$ (30 min) $\rightarrow {}^{15}NO/H_2/O_2/He$ (t) at 200 °C is made over the 0.1 wt% Pt/Ce$_{0.5}$Zr$_{0.5}$O$_{2-\delta}$ catalyst. The decay of Z_{Ar} (t) (Fig. 6) is used to monitor the gas phase hold-up from the switching valve to the MS detector system [24,25].

The concentration (μmol g^{-1}) of all the *active* adsorbed NO$_x$ species (named "N-pool") that participate in the reaction path from the gaseous NO to the formation of N$_2$ and N$_2$O is estimated by integrating the corresponding transient response curves of $^{14}N^{15}N$ and $^{14}N^{15}NO$ (inset graph, Fig. 6a) and those of $^{14}N_2$ and $^{14}N_2O$ with respect to the Ar curve and results are given in Table 2. The last column in Table 2 gives the size of the "N-pool" in terms of surface coverage, θ_N. The SSITKA-MS experiment was also performed at 250 °C for the H$_2$-SCR feed composition containing 15 vol% H$_2$O and the obtained result is also reported in Table 2 (number in parentheses). Values of θ greater than unity indicate that at least part of the active NO$_x$ cannot reside on Pt. For the present catalytic system, according to the SSITKA-DRIFTS results to be reported next (Section 3.3.1.2), all the active NO$_x$ reside within a zone around the Pt-support interface. Based on the concentration (μmol g^{-1}) of *active* NO$_x$ (Table 2), the extent (Δx, Å) of such a reactive zone around each Pt nanoparticle as depicted in Fig. 6b can be estimated. The latter quantity accounts for the number of Pt nanoparticles per gram of catalyst (number Pt g$_{cat}$$^{-1}$), the site density of oxygen anions and metal cations on the support surface (atoms nm^{-2}), the size of the hemispherical Pt nanoclusters (Table 1) and the concentration of active intermediates (mol g^{-1}, Table 2). The estimated values of Δx (Å) were found to be 1.45, 0.74 and 1.8 Å at 200, 250 and 300 °C, respectively. It is clear that in the reaction temperature range of 200–300 °C, Δx (Å) extends to less than *one lattice constant* of support from the Pt-support interface, thus, supporting the

view that the mode of bonding of *active* NO$_x$ largely involves the Pt-support interface.

A strong evidence that reduction of active NO$_x$ formed within a region near the metal-support interface of a Pt/CeO$_2$-MgO catalytic system proceeds through an H- spillover process, where Pt provides the H-spilt species, has been reported [27]. However, these H-spilt species cannot diffuse away from the Pt nanoparticle-support interface in a long distance according to transient isothermal DRIFTS-H$_2$ reduction experiments reported earlier [26].

The concentration of active NO$_x$ in the 200–300 °C range reported in Table 2 should be used to partly explain the activity behavior reported in Fig. 5a. The fact that the concentration of *active* NO$_x$ does not decrease monotonically in the 200–300 °C range (Table 2) provides a strong evidence that the monotonic decrease in the H$_2$-SCR rate observed for T ≥ 200 °C (Fig. 5a) must be related to other intrinsic kinetic reasons. We have previously reported [26] that the structure of active NO$_x$ may change with reaction T for the H$_2$-SCR on supported Pt. Therefore, an increase in the concentration of active NO$_x$ with T could be accompanied by a decreasing site reactivity of NO$_x$ due to the formation of different in chemical structure active NO$_x$ with T. Furthermore, the surface concentration of H is expected to decrease with increasing reaction T for two main reasons. First, as the reaction T increases, oxidation of surface Pt to PtO$_x$ does occur, thus decreasing the surface concentration of H. Secondly, the latter quantity is expected to decrease with reaction T as the result of the oxidation of H-s to water.

3.3.1.2. SSITKA-DRIFTS studies. The chemical structure of the *active* NO$_x$ species that truly participate in the nitrogen reaction path of the H$_2$-SCR of NO was studied by SSITKA-DRIFTS. A DRIFT spectrum was first recorded after 30 min of reaction in the $^{14}NO/H_2/O_2$ gas mixture. The reaction feed stream was then switched to the equivalent isotopic $^{15}NO/H_2/O_2$ gas mixture and after 30 min of reaction (new steady state) a DRIFT spectrum was recorded. Fig. 7 shows *in situ* SSITKA-DRIFT spectra recorded in the 1700–950 cm^{-1} range over the 0.1 wt% Pt/Ce$_{0.5}$Zr$_{0.5}$O$_{2-\delta}$ catalyst at 200 °C. IR bands that shift to lower wavenumbers after the isotopic switch (^{15}N—O vs ^{14}N—O stretching vibrational mode) correspond very likely to *active* adsorbed NO$_x$ reaction intermediates formed during the NO/H$_2$/O$_2$ reaction which lead to N$_2$ and N$_2$O gas products [5,25–28]. On the other hand, IR bands which do not provide the red isotopic shift correspond to *inactive* (spectator) adsorbed NO$_x$ species.

After deconvolution of the spectral region shown in Fig. 7 (solid line), only two IR bands provided the red isotopic shift as depicted
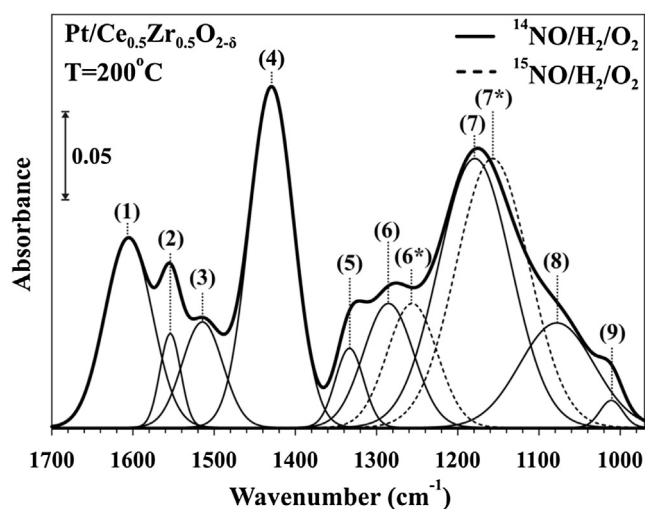
Fig. 7. *In situ* SSITKA-DRIFT spectra recorded in the 1700–950 cm^{-1} range over 0.1 wt% Pt/Ce$_{0.5}$Zr$_{0.5}$O$_{2-\delta}$ during H$_2$-SCR at 200 °C under 150 ppm ^{14}NO/0.8 vol% H$_2$/2.5 vol% O$_2$/He (solid spectra) and 150 ppm ^{15}NO/0.8 vol% H$_2$/2.5 vol% O$_2$/He (dashed spectra) feed gas mixtures. Deconvolution of the recorded IR spectra is also shown.

Fig. 8. *In situ* DRIFT spectra recorded in the 3050–2750 cm^{-1} range over 0.1 wt% Pt/Ce$_{0.5}$Zr$_{0.5}$O$_{2-\delta}$ at 200 °C under different feed gas compositions for probing the formation of adsorbed −CH$_x$ species. Feed gas compositions: (i) 150 ppm NO/0.8 vol% H$_2$/2.5 vol% O$_2$/He; (ii) 150 ppm NO/0.5 vol% C$_3$H$_6$/2.5 vol% O$_2$/He; (iii) 0.5 vol% C$_3$H$_6$/2.5 vol% O$_2$/He; (iv) 150 ppm NO/0.8 vol% H$_2$/0.5 vol% C$_3$H$_6$/2.5 vol% O$_2$/He; (v) 0.5 vol% CO$_2$/10 vol% H$_2$O/2.5 vol% O$_2$/He.

by the dashed-line spectra. The IR bands centered at 1605, 1557 and 1068 (band 1, 2 and 8) correspond to the νNO$_{2(as)}$, νNO$_{2(sym)}$ and νN−O vibrational modes of *bidentate nitrate* formed on the support, whereas those centered at 1506, 1315 and 1021 cm^{-1} (band 3, 5 and 9) to the same vibrational modes of the *monodentate nitrate* also residing on the support. The IR bands recorded at 1280 and 1182 cm^{-1} (bands 6 and 7) are attributed to the asymmetric (ν_{as}) and symmetric (ν_{sym}) N−O stretching mode of the *chelating nitrite* (NO$_2^-$), while band 4 (1434 cm^{-1}) is assigned to adsorbed *nitrosyl* (NO$_2^+$) on the Ce-Zr-O mixed metal oxide. The assignment of the various adsorbed NO$_x$ species was based on well-documented literature data [26,27,50–57]. As depicted in Fig. 7, only the IR bands due to a *chelating nitrite* species (band 6 and 7) showed the *red isotopic shift* upon replacing the ^{14}N with ^{15}N in the "nitrogen-path" of the H$_2$-SCR (bands labelled with *). In order to exclude the possibility that the isotopic shift provided by the chelating nitrites is not the result of a simple exchange of ^{15}NO with ^{14}NO$_2^-$, after H$_2$-SCR (^{14}NO/H$_2$/O$_2$) at 200 °C, the feed was switched to 150 ppm ^{15}NO/Ar for 30 min and a spectrum was then recorded. There was not any isotopic shift for the specific bands associated with the chelating nitrite species. The latter results strongly suggest that chelating nitrite is the *active intermediate* that is involved in the H$_2$-SCR mechanism, whereas nitrosyls, monodentate and bidentate nitrates must be considered as *inactive species* (spectators). Similar results were also reported over the Pt/CeO$_2$-MgO catalyst [26], where *two* active NO$_x$ intermediate species were identified; one in the vicinity of the Pt-CeO$_2$ support interface (*nitrosyl* [NO$^+$] *coadsorbed with nitrate* [NO$_3^-$] on adjacent Ce^{4+}-oxygen anion site pair) and the other one located in the vicinity of the Pt-MgO support interface. The chemical structure of the *active* NO$_x$ species was found to depend on reaction temperature [26].

3.3.2. Selective catalytic reduction of NO using H$_2$/C$_3$H$_6$

3.3.2.1. In situ DRIFTS studies.
Fig. 8 shows IR bands in the 2750–3050 cm^{-1} range recorded over the 0.1 wt% Pt/Ce$_{0.5}$Zr$_{0.5}$O$_{2-\delta}$ at 200 °C under different feed gas compositions and which are attributed to the asymmetric and symmetric νC−H stretching vibrations in CH$_x$ groups of hydrocarbon fragments adsorbed on the Pt surface. The IR bands centered at 2956 (band 1) and 2870 cm^{-1} (band 3) are assigned to the asymmetric and symmetric CH stretch (νCH) of CH$_3$ group, whereas the IR band at 2932 cm^{-1} (band 2)
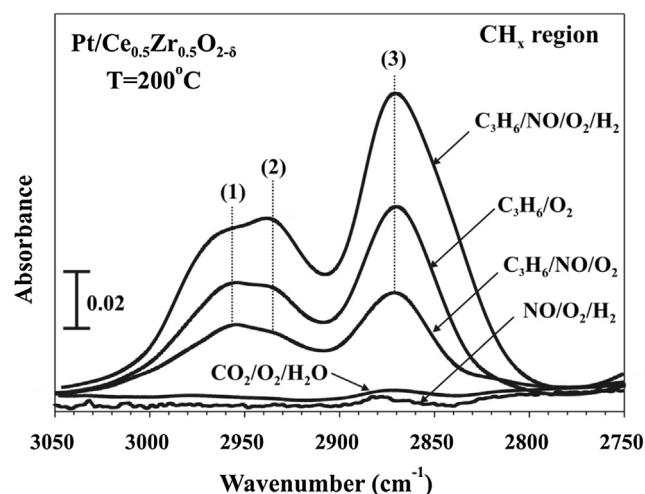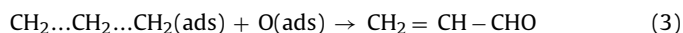
to the symmetric CH stretch (νCH) of CH$_2$ group [58–64]. It is important to note that under pretreatment of the catalyst with the CO$_2$/O$_2$/H$_2$O gas mixture, the characteristic νCH and δCH vibrational modes of adsorbed formate (HCOO-) were not observed, strongly suggesting that the IR bands 1–3 (Fig. 8) should only be assigned to −CH$_x$ adsorbed species arising from the interaction of C$_3$H$_6$ with the catalyst surface. It is clearly seen that the −CH$_x$ hydrocarbon fragments are not observed under the H$_2$-SCR gas mixture (NO/H$_2$/O$_2$) but they do appear under the C$_3$H$_6$/O$_2$ reaction gas mixture. Adsorption of propylene on metal and oxidic surfaces forms π-allyl complexes, whereas subsequent interaction with oxygen leads to partial oxidation and formation of acrolein [60,65]:

$$CH_3 - CH = CH_2 \rightarrow CH_2...CH_2...CH_2(ads) + H(ads) \tag{2}$$

$$CH_2...CH_2...CH_2(ads) + O(ads) \rightarrow CH_2 = CH - CHO \tag{3}$$

Further oxidation of acrolein leads to the formation of −COO$^-$ and −CH$_x$ fragments from an initially formed acrylate-type intermediate species (C$_x$H$_y$O$_z$). In the case of C$_3$H$_6$-SCR (NO/C$_3$H$_6$/O$_2$), the surface concentration of adsorbed −CH$_x$ species is reduced compared with that obtained in the absense of NO in the feed (Fig. 8). The latter provides evidence of possible interaction of adsorbed −CH$_x$ with NO during C$_3$H$_6$-SCR. According to previous works [2,59,60,66–68], the interactions of adsorbed NO and C$_x$H$_y$O$_z$ species (unknown chemical structure) are key steps of C$_3$H$_6$-SCR. In the present DRIFTS work it was not possible to identify any −CHN or −CN intermediates in the 200–400 °C range. It is to be mentioned, however, that the behavior of the IR band intensities with the various gas atmospheres obtained at 400 °C was similar to that obtained at 200 °C (Fig. 8) except that the measured integral absorbance intensities were significantly lower.

According to the results shown in Fig. 8, the steady-state surface coverage of adsorbed −CH$_x$ species derived from the decomposition of propylene at 200 °C and which occurred largely on Pt, is found to increase under C$_3$H$_6$/H$_2$-SCR compared to the C$_3$H$_6$-SCR, in harmony with the de-NO$_x$ activity behaviour (Fig. 5a). As will be shown in the following section, this might be related to the formation of new active species (CH$_x$-NO$_2$) the reactivity of which is enhanced in the presence of hydrogen. As clearly illustrated in the catalytic results of Fig. 5a, hydrogen appears as a
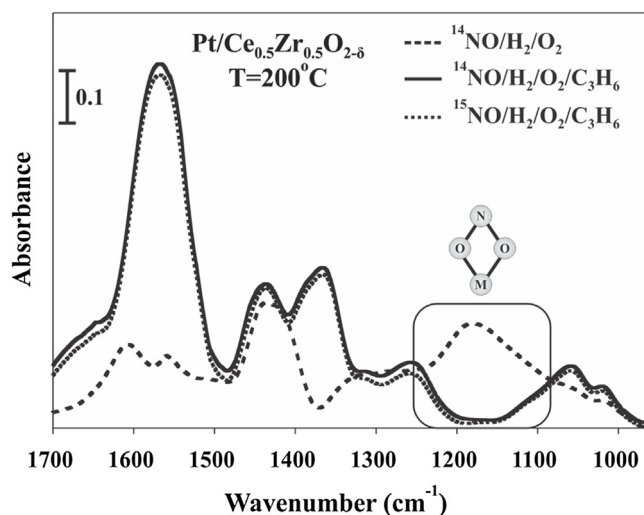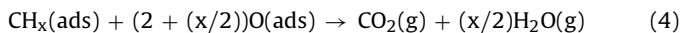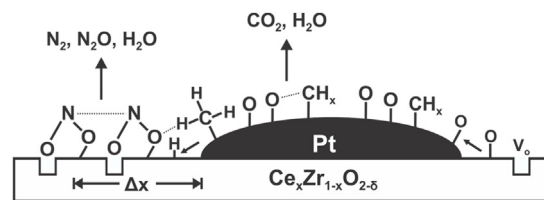
Fig. 9. *In situ* SSITKA-DRIFT spectra recorded in the 1700–950 cm^{-1} range over 0.1 wt% Pt/Ce$_{0.5}$Zr$_{0.5}$O$_{2-\delta}$ during C$_3$H$_6$/H$_2$-SCR at 200 °C. The DRIFT spectrum obtained during H$_2$-SCR is also shown. Feed gas compositions: (i) 150 ppm ^{14}NO/0.5 vol% C$_3$H$_6$/0.8 vol% H$_2$/2.5 vol% O$_2$/He (−); (ii) 150 ppm ^{15}NO/0.5 vol% C$_3$H$_6$/0.8 vol% H$_2$/2.5 vol% O$_2$/He (⋯); (iii) 150 ppm ^{14}NO/0.8 vol% H$_2$/2.5 vol% O$_2$/He (----).

stronger reducing agent than propylene at reaction temperatures lower than 300 °C. On the other hand, the intensity of the IR bands under the experiments described in Fig. 8 may not be strictly related to *active* adsorbed intermediate species only but also partly to inactive species. In fact, the increase in the −CH$_x$ concentration should be seen as controlled by the rate of its formation via propylene dissociative chemisorption and its rate of consumption via CH$_x$-NO$_2$ and combustion by adsorbed O species (Eq. (4)):

$$CH_x(ads) + (2 + (x/2))O(ads) \rightarrow CO_2(g) + (x/2)H_2O(g) \qquad (4)$$

A strong C$_3$H$_6$-induced blocking effect of Pd and Pd-support interface sites was reported over Pd supported on 15 wt% CeO$_2$-ZrO$_2$/γ-Al$_2$O$_3$ carrier three-way catalyst tested towards C$_3$H$_6$/CO-SCR and CO-SCR, where hindering of CO adsorption was observed on Pd [69]. The authors contributed this effect on the strong chemisorption of propylene and its decomposition fragments on the Pd particles. Furthermore, using in situ DRIFTS, a C$_3$H$_6$-induced blocking effect of sites at the support and in the formation of −NCO species on Pd were evident [69]. On the basis of the DRIFTS results of Fig. 8 and the NO-conversion behavior in the 200–400 °C range (Fig. 5a), even though the −CH$_x$ concentration under C$_3$H$_6$/H$_2$-SCR is larger than that under C$_3$H$_6$-SCR, thus apparently blocking a larger concentration of surface Pt sites, the surface concentration of H and its rate of diffusion towards the active NO$_x$ located at the Pt-support interface, an important step for H$_2$-SCR [26–28], is only little affected.

3.3.2.2. SSITKA-DRIFTS studies.

Fig. 9 shows DRIFT spectra recorded over the 0.1 wt% Pt/Ce$_{0.5}$Zr$_{0.5}$O$_{2-\delta}$ catalyst 30 min before (continuous line) and after (dotted line) the SSITKA switch ^{14}NO/H$_2$/C$_3$H$_6$/O$_2$/He → ^{15}NO/H$_2$/C$_3$H$_6$/O$_2$/He was made at 200 °C. For comparison, the spectrum obtained under H$_2$-SCR (NO/H$_2$/O$_2$, dashed line) is also shown. In the case of C$_3$H$_6$/H$_2$-SCR, the 1700–950 cm^{-1} spectral region besides the characteristic vibrational modes of adsorbed NO$_x$ species may also exhibit O−C−O stretching vibrational modes due to formate, carbonate or carboxylate species onto the metal or support surface. According to the results shown in Fig. 9, none of the IR bands due to adsorbed NO$_x$ provided the red isotopic shift for the N−O stretching vibrational mode. Furthermore, it is seen that the IR band at 1182 cm^{-1} (Fig. 7,

band 7) due to the *chelating nitrite* (NO$_2^-$) species *is not observed* under C$_3$H$_6$/H$_2$-SCR. It is, therefore, suggested that when C$_3$H$_6$ is co-fed with H$_2$, the intrinsic activity of the *chelating nitrite* active species under H$_2$-SCR is enhanced, leading to a non-measurable surface coverage. This result could provide a reasonable link to the high NO conversion and N$_2$-selectivity values observed at T > 450 °C (Fig. 5). It should be made clear at this point that at least one active adsorbed NO$_x$ species must be present under the C$_3$H$_6$/H$_2$-SCR.

Azambre et al. [70] have investigated the interaction of NO/NO$_2$ with the surface of Ce$_{0.76}$Zr$_{0.24}$O$_2$ solids at 350 °C by DRIFTS. The spectra were dominated by the presence of bidentate or chelating nitrites, as revealed by the broad and strong *asymmetric* N−O mode centered in the 1194–1160 cm^{-1} range. This result is in agreement with the results shown in Figs. 7 and 9 at 200 °C. It was reported [70] that the symmetric mode (1270–1260 cm^{-1}) cannot be easily detected due to its weak intensity and overlapping with vibrations due to nitrate species. This result is in harmony with what is observed in Fig. 9, where in spite of the absence of the asymmetric mode of chelating nitrite under C$_3$H$_6$/H$_2$-SCR, the IR band centered at ∼1260 cm^{-1} does appear due to the presence of an *inactive* (spectator) nitrate species. Furthermore, it was reported that *nitrites* are formed on reduced centers of ceria and Ce$_{1-x}$Zr$_x$O$_2$ surfaces after the interaction with NO$_2$ (Eq. (5)), the latter formed by NO oxidation on other surface sites, where an electron is transferred from a Ce^{3+} reduced center to the NO$_2$ adsorbed species:

$$Ce^{3+}-\square + NO_2 \rightarrow Ce^{4+} - ONO^- \qquad (5)$$

For the present supported Pt catalyst and the lean de-NO$_x$ reaction conditions applied, formation of NO$_2$ can also take place on the Pt surface [71,72].

A significant increase of the IR bands recorded at 1560 and 1375 cm^{-1} and which are attributed to acrylate-type species (C$_x$H$_y$O$_z$) [58–64] is observed under C$_3$H$_6$/H$_2$-SCR (Fig. 9) and the new IR band (shoulder) recorded at 1650 cm^{-1} (Fig. 9) is assigned to adsorbed CH$_x$-NO$_2$. Due to the large overlapping of the latter IR band with that at 1560 cm^{-1}, it was difficult to identify an isotopic shift for this particular band. Therefore, based on the disappearance of NO$_2^-$ and appearance of CH$_x$-NO$_2$, it is suggested that the latter species might be considered as another active reaction intermediate that leads exclusively to N$_2$ at T > 450 °C under C$_3$H$_6$/H$_2$-SCR.

3.3.2.3. Synergy effect in the H$_2$/C$_3$H$_6$-SCR on Pt/Ce$_{1-x}$Zr$_x$O$_{2-\delta}$.

Scheme 1 depicts essential mechanistic features of the C$_3$H$_6$/H$_2$-SCR of NO in the 200–600 °C range over the 0.1 wt% Pt/Ce$_{0.5}$Zr$_{0.5}$O$_{2-\delta}$ catalyst based on the results of the present work that capture the strong synergy effect observed between C$_3$H$_6$ and H$_2$ reducing agents in the SCR of NO at T > 400 °C. It is important to recall at this point that the presence of H$_2$ in the lean de-NO$_x$ reaction mixture is that which plays the major role in the activity behavior of the present catalytic system based on the activity behavior shown in Fig. 5a. In the case of C$_3$H$_6$-SCR, at T > 400 °C the NO-conversion is lower than 20%, whereas in the case of H$_2$-SCR this takes values in the 45–70%-range (Fig. 5a). When both reducing agents are present in the feed stream, a boost in X$_{NO}$ takes place at T > 400 °C

Scheme 1. Main mechanistic features of C$_3$H$_6$/H$_2$-SCR of NO over the Pt/Ce$_{0.5}$Zr$_{0.5}$O$_{2-\delta}$ catalyst; V$_O$: oxygen vacant site.

(practically complete conversion of NO), whereas in the lower temperature range of 200–400 °C, the NO conversion follows closely that of H_2-SCR (Fig. 5a).

The SSITKA-MS investigation allowed the quantitative determination of the *active* NO_x species formed during H_2-SCR (Table 2), result that points out that these species must largely reside at the metal-support interface or within a region extending by no more than *one lattice constant* within the support surface. Thus, a plausible mechanistic step for the reduction of NO_x located within a zone around the metal-support interface is that of *hydrogen spillover* from the Pt to the support surface according also to previous findings over the Pt/MgO-CeO$_2$ [21,26,27], Pt/SiO$_2$ [73], Pt/La$_{0.5}$Ce$_{0.5}$MnO$_3$ [28,74] and Pt/La$_{0.7}$Sr$_{0.2}$Ce$_{0.1}$FeO$_3$ [75] catalysts.

Wang et al. [6] in their recent elegant TAP work on lean de-NO$_x$ on (La, Zr)-doped CeO$_2$ have found that at 560 °C the role of carbonaceous –CH$_x$ deposits after pretreatment with C$_3$H$_6$ was to create *active oxygen anion defects* by the oxidation of these carbonaceous species to CO$_2$ and H$_2$O. These active support oxygen vacancies enabled substantial additional NO reduction selectively towards N$_2$ formation. They have also reported [6] that after C$_3$H$_6$ reduction pre-treatment of the solid, the N-accumulation was 1.6 times higher compared to that of H$_2$ reduction pre-treatment. On the basis of the above results, the *promoting role* of H$_2$ in boosting the de-NO$_x$ activity over the present 0.1 wt% Pt/Ce$_{0.5}$Zr$_{0.5}$O$_{2-\delta}$ catalyst at temperatures larger than 450 °C (Fig. 5a, Section 3.2.1) might be linked to the enhanced combustion of –CH$_x$ at high temperatures by labile oxygen present in the Ce$_{0.5}$Zr$_{0.5}$O$_{2-\delta}$ support, the rate of diffusion of it on the Pt surface to be enhanced by the lowering of adsorbed oxygen concentration on Pt due to its removal by adsorbed atomic H according to Eqs. (6)–(7), enhancing, therefore, the rate of oxygen back-spillover towards the Pt surface.

$$H_2(g) \rightarrow 2\,H(ads) \tag{6}$$

$$2\,H(ads) + O(ads) \rightarrow H_2O(g) \tag{7}$$

Chelating nitrite (NO_2^-) being very likely an *active* NO_x species in the C$_3$H$_6$/H$_2$-SCR, according to the SSITKA-DRIFTS studies (Section 3.3.2.2), appears now to be more active when one of its oxygen atoms is associated with an oxygen vacant site (Eq. (5), weakening of the N—O bonding) as compared to the case of H$_2$-SCR (see Section 3.3.1.2) and it largely contributes to the selective reduction of NO_x to N$_2$(g) at high temperatures (see Fig. 5, T > 400 °C). It might be considered that adsorbed –CH$_x$ partly blocks active sites for oxygen chemisorption, thus increasing the surface coverage of H-s. The latter quantity is mainly determined by the rate of dissociative hydrogen chemisorption on Pt under reaction conditions (partly oxidized) and to a lesser extent from –CH$_x$ decomposition. The latter is true based on the activity behavior of H$_2$-SCR and C$_3$H$_6$-SCR at T > 400 °C (Fig. 5a). These steps contribute then to the increase in the rate of removal of O-s on Pt (via the formation of H$_2$O) and in turn in the rate of *oxygen back spillover* from the reducible Ce$_{1-x}$Zr$_x$O$_{2-\delta}$ support surface to the Pt metal. The latter is then equivalent to the *enhancement of the rate of formation of oxygen vacant sites* on the support (within the active zone around the Pt nanoparticles as previously discussed). This result is suggested to be the *origin of the synergy* between the two reducing agents under the present SCR conditions.

Maunula et al. [76] have studied the H$_2$-SCR reaction mechanism over a Pt/CeO$_2$-Al$_2$O$_3$ catalyst using various transient experiments. They reported that an *active* NO_x intermediate is likely that of (NO)$_2$ dimer designated as *NO···NO*. This can lead either to N$_2$O and atomic oxygen or to N$_2$ and atomic oxygen. In the present work it is suggested that two adjacent NO_x species of the same chemical structure (chelating nitrite) and which are not formed on Pt but on the support surface are reduced by either spilt H atoms from the Pt to the support or by CH$_x$ species via an adsorbed C$_x$H$_y$O$_z$

intermediate. For the former case, the surface diffusion of H on Pt towards the NO_x adsorption site within the active reaction zone around the Pt nanoparticles becomes important. The production of CO$_2$ and H$_2$O is the result of the oxidation of CH$_x$ by adsorbed oxygen on the Pt surface (Eq. (4)), where water formation is also the result of the reduction of adsorbed NO_x by hydrogen.

The results of the present transient isotopic and *in situ* DRIFTS investigations on the Pt/Ce$_{0.5}$Zr$_{0.5}$O$_{2-\delta}$ catalytic system towards lean de-NO$_x$ using H$_2$ and C$_3$H$_6$ as reducing agents provided a better understanding of important kinetic steps of NO transformation that will help to bring further improvements towards the design of suitable and robust catalytic systems for de-NO$_x$ processes using environmentally benign reducing agents such as hydrogen.

4. Conclusions

The following conclusions can be derived from the results of the present work:

(a) The Pt/Ce$_{0.5}$Zr$_{0.5}$O$_{2-\delta}$ solid exhibits remarkable "activity window" of operation in the 180–300 °C range (X_{NO} > 80%) with S_{N2} in the 60–75% range under H$_2$-SCR (150 ppm NO, 2.5% O$_2$) but in the absence of CO$_2$ and H$_2$O in the feed stream. The presence of the latter two gases in the feed stream (practical lean burn conditions) causes significant loss of activity and N$_2$-selctivity.

(b) When both H$_2$ and C$_3$H$_6$ were used as reducing agents towards SCR of NO (150 ppm NO, 2.5% O$_2$), a remarkable strong *synergy effect* in the temperature range of 400–600 °C was observed. The latter resulted in complete conversion of NO and N$_2$-selectivity values larger than 97%. This *synergy effect* between H$_2$ and C$_3$H$_6$ was explained to arise mainly due to: (i) the increase of the surface coverage of adsorbed H by the presence of –CH$_x$ species (derived from propylene chemisorption) which block sites of oxygen chemisorption on Pt. Atomic hydrogen is an important intermediate for the reduction of adsorbed active NO_x located within a region of support around the Pt nanoparticles; (ii) the increase of surface oxygen vacant sites within the reactive region due to the increase in the rate of back spillover of labile oxygen (reducible Ce$_{1-x}$Zr$_x$O$_{2-\delta}$ support) as the result of a lower surface coverage of oxygen on Pt; (iii) the increased site reactivity of chelating nitrite species formed via the participation of an oxygen vacancy compared to the case of H$_2$-SCR alone.

(c) It was proved *for the first time* that the active NO_x that participate in the H$_2$-SCR path using realistic lean burn conditions: 150 ppm NO, 2.5%O$_2$, 0.8% H$_2$ reside within a reactive zone around each Pt nanoparticle that extends to *less than one lattice constant* within the support surface. Only the *chelating nitrite* species was found to be an active intermediate, whereas nitrosyls, monodentate and bidentate nitrates were found to be *inactive* species (spectators).

(d) Based on SSITKA-MS experiments it was proved *for the first time* that the presence of H$_2$O in the feed stream results into a 25% decrease in the *active* N-containing intermediate species, result that partly explains the significant drop of activity when water is present in the feed stream of H$_2$-SCR.

References

[1] R. Burch, P.J. Millington, A.P. Walker, Appl. Catal. B: Environ. 4 (1994) 65–94.

[2] M.D. Amiridis, T. Zhang, R. Farrauto, Appl. Catal. B: Environ. 10 (1996) 203–227.
[3] R. Burch, J.P. Breen, F.C. Meunier, Appl. Catal. B: Environ. 39 (2002) 283–303.
[4] P. Granger, V.I. Parvulescu, Chem. Rev. 111 (2011) 3155–3207.
[5] A.M. Efstathiou, V.N. Stathopoulos, Chapter 26–lean burn DeNO$_x$ applications: stationary and mobile sources, in: P. Granger, V.I. Parvulescu, S. Kaliaguine, W. Prellier (Eds.), Perovskites and Related Mixed Oxides: Concepts and Applications, Wiley-VCH, 2016, pp. 587–610.
[6] Y. Wang, J. Posthuma de Boer, F. Kapteijn, M. Makkee, ChemCatChem 8 (2016) 102–105.
[7] M.P. Harold, Curr. Opin. Chem. Eng. 1 (2012) 303–311.
[8] J.P. Breen, R. Burch, C. Hardacre, C.J. Hill, J. Phys. Chem. B 109 (2005) 4805–4807.
[9] J.P. Breen, R. Burch, C. Hardacre, C.J. Hill, C. Rioche, J. Catal. 246 (2007) 1–9.
[10] S. Satokawa, Chem. Lett. 29 (2000) 294–295.
[11] U. Bentrup, M. Richter, R. Fricke, Appl. Catal. B: Environ. 55 (2005) 213–220.
[12] K. Eränen, F. Klingstedt, K. Arve, L.-E. Lindfors, D.Y. Murzin, J. Catal. 227 (2004) 328–343.
[13] S. Satokawa, J. Shibata, K.-i. Shimizu, A. Satsuma, T. Hattori, Appl. Catal. B: Environ. 42 (2003) 179–186.
[14] K.-I. Shimizu, A. Satsuma, Phys. Chem. Chem. Phys. 8 (2006) 2677–2695.
[15] M.A. Goula, N.D. Charisou, K.N. Papageridis, A. Delimitis, E. Papista, E. Pachatouridou, E.F. Iliopoulou, G. Marnellos, M. Konsolakis, I.V. Yentekakis, J. Environ. Chem. Eng. 4 (2016) 1629–1641.
[16] C.N. Costa, A.M. Efstathiou, Appl. Catal. B: Environ. 72 (2007) 240–252.
[17] A. Väliheikki, K.C. Petallidou, C.M. Kalamaras, T. Kolli, M. Huuhtanen, T. Maunula, R.L. Keiski, A.M. Efstathiou, Appl. Catal. B: Environ. 156–157 (2014) 72–83.
[18] L. Masdrag, X. Courtois, F. Can, S. Royer, E. Rohart, G. Blanchard, P. Marecot, D. Duprez, Catal. Today 189 (2012) 70–76.
[19] C.N. Costa, T. Anastasiadou, A.M. Efstathiou, J. Catal. 194 (2000) 250–265.
[20] M.M. Makri, M.A. Vasiliades, K.C. Petallidou, A.M. Efstathiou, Catal. Today 259 (2015) 150–164.
[21] C.N. Costa, A.M. Efstathiou, Appl. Catal. B: Environ. 72 (2007) 240–252.
[22] G.G. Olympiou, A.M. Efstathiou, Chem. Eng. J. 170 (2011) 424–432.
[23] B.C. Smith, Fundamentals of Fourier Transform Infrared Spectroscopy, CRC Press, Boca Raton, FL, 1996.
[24] A.M. Efstathiou, X.E. Verykios, Appl. Catal. A: Gen. 151 (1997) 109–166.
[25] A.M. Efstathiou, J.T. Gleaves, G.S. Yablonsky, Chapter 22–transient techniques: temporary analysis of products (TAP) and steady state isotopic transient kinetic analysis (SSITKA), in: M. Che, J.C. Vedrine (Eds.), Characterization of Solid Materials: From Structure to Surface Reactivity, Wiley-VCH, 2012, pp. 1013–1073.
[26] P.G. Savva, A.M. Efstathiou, J. Catal. 257 (2008) 324–333.
[27] C.N. Costa, A.M. Efstathiou, J. Phys. Chem. C 111 (2007) 3010–3020.
[28] C.N. Costa, A.M. Efstathiou, J. Phys. Chem. B 108 (2004) 2620–2630.
[29] X. Wang, G. Lu, Y. Guo, Y. Xue, L. Jiang, Y. Guo, Z. Zhang, Catal. Today 126 (2007) 412–419.
[30] M.Y. Youn, J.G. Seo, K.M. Cho, S. Park, D.R. Park, J.C. Jung, I.K. Song, Int. J. Hydrogen Energy 33 (2008) 5052–5059.
[31] M. Yashima, K. Morimoto, N. Ishizawa, M. Yoshimura, J. Amer. Ceram. Soc. 76 (1993) 1745–1750.
[32] C.E. Hori, H. Permana, K.Y.S. Ng, A. Brenner, K. More, K.M. Rahmoeller, D. Belton, Appl. Catal. B: Environ. 16 (1998) 105–117.
[33] S. Rossignol, Y. Madier, D. Duprez, Catal. Today 50 (1999) 261–270.
[34] G. Gouadec, P. Colomban, Prog. Cryst. Growth Charact. Mater. 53 (2007) 1–56.
[35] D.A. Daramola, M. Muthuvel, G.G. Botte, J. Phys. Chem. B 114 (2010) 9323–9329.
[36] J.R. McBride, K.C. Hass, B.D. Poindexter, W.H. Weber, J. Appl. Phys. 76 (1994) 2435–2441.
[37] S. Letichevsky, C.A. Tellez, R.R. de Avillez, M.I.P. Da Silva, M.A. Fraga, L.G. Appel, Appl Catal B: Environ. 58 (2005) 203–210.
[38] F. Zhang, C.-H. Chen, J. Amer. Ceram. Soc. 89 (2006) 1028–1036.
[39] M. Yashima, H. Arashi, M. Kakihana, M. Yoshimura, J. Amer. Ceram. Soc. 77 (1994) 1869–1874.
[40] I. Van Zandvoort, Y. Wang, B.C. Rasrendra, E.R.H. van Eck, P.C.A. Bruijnincx, H.J. Heeres, B.M. Weckhuysen, Formation, molecular structure, and morphology of humins in biomass conversion: influence of feedstock and processing condition, ChemSusChem 6 (2013) 1745–1758.
[41] J. Rynkowski, J. Farbotko, R. Touroude, L. Hilaire, Appl. Catal. A: Gen. 203 (2000) 335–348.
[42] H. He, H.X. Dai, L.H. Ng, K.W. Wong, C.T. Au, J. Catal. 206 (2002) 1–13.
[43] X. Wu, L. Xu, D. Weng, Appl. Surf. Sci. 221 (2004) 375–383.
[44] D.I. Kondarides, X.E. Verykios, J. Catal. 174 (1998) 52–64.
[45] S. Ricote, G. Jacobs, M. Milling, Y. Ji, P.M. Patterson, B.H. Davis, Appl. Catal. A: Gen. 303 (2006) 35–47.
[46] X. Wang, G. Lu, Y. Guo, Y. Xue, L. Jiang, Y. Guo, Z. Zhang, Catal. Today 126 (2007) 412–419.
[47] A.E. Nelson, K.H. Schulz, Appl. Surf. Sci. 210 (2003) 206–221.
[48] J.Z. Shyu, W.H. Weber, H.S. Gandhi, J. Phys. Chem. 92 (1988) 4964–4970.
[49] X. Liu, K. Zhou, L. Wang, B. Wang, Y. Li, J. Am. Chem. Soc. 131 (2009) 3140–3141.
[50] B. Klingenberg, M.A. Vannice, Appl. Catal. B: Environ. 21 (1999) 19–33.
[51] K.I. Hadjiivanov, Catal. Rev. 42 (2000) 71–144.
[52] J. Müslehiddinoğlu, M.A. Vannice, J. Catal. 217 (2003) 442–456.
[53] S.J. Huang, A.B. Walters, M.A. Vannice, J. Catal. 192 (2000) 29–47.
[54] A. Bourane, O. Dulaurent, S. Salasc, C. Sarda, C. Bouly, D. Bianchi, J. Catal. 204 (2001) 77–88.
[55] T.E. Hoost, K. Otto, K.A. Laframboise, J. Catal. 155 (1995) 303–311.
[56] J.-L. Freysz, J. Saussey, J.-C. Lavalley, P. Bourges, J. Catal. 197 (2001) 131–138.
[57] K. Hadjiivanov, M. Mihaylov, D. Panayotov, E. Ivanova, K. Chakarova, Spectrosc. Prop. Inorg. Organomet. Compd. 45 (2014) 43.
[58] T.E. Hoost, K.A. Laframboise, K. Otto, Appl. Catal. B: Environ. 7 (1995) 79–93.
[59] Z. Zhang, M. Chen, Z. Jiang, W. Shangguan, J. Environ. Sci. 22 (2010) 1441–1446.
[60] T.I. Halkides, D.I. Kondarides, X.E. Verykios, Catal. Today 73 (2002) 213–221.
[61] R. da Silva, R. Cataluña, A. Martínez-Arias, Catal. Today 143 (2009) 242–246.
[62] I.A. Ransley, L.M. Ilharco, J.E. Bateman, B.H. Sakakini, J.C. Vickerman, M.A. Chesters, Sur. Sci. 298 (1993) 187–194.
[63] T. Beutel, B. Adelman, W.M.H. Sachtler, Catal. Lett. 37 (1996) 125–130.
[64] M.A. Chesters, C. De La Cruz, P. Gardner, E.M. McCash, P. Pudney, G. Shahid, N. Sheppard, J. Chem. Soc. Faraday Trans. 86 (1990) 2757–2763.
[65] V.A. Matyshak, O.V. Krylov, Catal. Today 25 (1995) 1–87.
[66] A. Fritz, V. Pitchon, Appl. Catal. B: Environ. 13 (1997) 1–25.
[67] V.I. Pârvulescu, P. Grange, B. Delmon, Catal. Today 46 (1998) 233–316.
[68] A. Obuchi, A. Ohi, M. Nakamura, A. Ogata, K. Mizuno, H. Ohuchi, Appl. Catal. B: Environ. 2 (1993) 71–80.
[69] A. Martínez-Arias, M. Fernández-Garcia, A.B. Hungría, A. Iglesias-Juez, K. Duncan, R. Smith, J.A. Anderson, J.C. Conesa, J. Soria, J. Catal. 204 (2001) 238–248.
[70] B. Azambre, I. Atribak, A. Bueno-López, A. García-García, J. Phys. Chem. C 114 (2010) 13300–13312, references therein.
[71] K. Leistner, A. Nicolle, P. Da Costa, Appl. Catal. B: Environ. 111–112 (2012) 415–423.
[72] Y. Ji, T.J. Toops, U.M. Graham, G. Jacobs, M. Crocker, Catal. Lett. 110 (2006) 29–37.
[73] R. Burch, A.A. Shestov, J.A. Sullivan, J. Catal. 188 (1999) 69–82.
[74] C.N. Costa, V.N. Stathopoulos, V.C. Belessi, A.M. Efstathiou, J. Catal. 197 (2001) 350–364.
[75] C.N. Costa, P.G. Savva, C. Andronikou, P.S. Lambrou, K. Polychronopoulou, V.C. Belessi, V.N. Stathopoulos, P.J. Pomonis, A.M. Efstathiou, J. Catal. 209 (2002) 456–471.
[76] T. Maunula, J. Ahola, T. Salmi, H. Haario, M. Härkönen, M. Luoma, V.J. Pohjola, Appl. Catal. B: Environ. 12 (1997) 287–308.